The Simulation of Magnetic Resonance Elastography through Atherosclerosis

The Simulation of Magnetic Resonance Elastography through Atherosclerosis

L. E. J. Thomas-Seale[1*], L. Hollis[1], D. Klatt[2], I. Sack[2], N. Roberts[3], P. Pankaj[4] and P. R. Hoskins[1]

[1]*Centre for Cardiovascular Science, University of Edinburgh, Queen's Medical Research Institute, 47 Little France Crescent, Edinburgh, UK.*

[2]*Department of Radiology, Charité - Universitätsmedizin Berlin, Berlin, Germany*

[3]*Clinical Research Imaging Centre, University of Edinburgh, 47 Little France Crescent, Edinburgh, UK.*

[4]*School of Engineering, University of Edinburgh, Alexander Graham Bell Building, The King's Buildings, Edinburgh, UK.*

* *Corresponding Author*

Address: Department of Mechanical Engineering, School of Engineering, University of Birmingham, Edgbaston, Birmingham, B15 2TT

Email: Email: l.e.j.thomas-seale@bham.ac.uk / lauren.ej.thomas.seale@gmail.com

Phone: (+44) 0121 4143622 / (+44) 07841 515310

Keywords: Atherosclerosis, Elastography, FEA, MRE.

Abstract

The clinical diagnosis of atherosclerosis via the measurement of stenosis size is widely acknowledged as an imperfect criterion. The vulnerability of an atherosclerotic plaque to rupture is associated with its mechanical properties. The potential to image these mechanical properties using magnetic resonance elastography (MRE) was investigated through synthetic datasets.

An image of the steady state wave propagation, equivalent to the first harmonic, can be extracted directly from finite element analysis. Inversion of this displacement data yields a map of the shear modulus, known as an elastogram. The variation of plaque composition, stenosis size, Gaussian noise, filter thresholds and excitation frequency were explored.

A decreasing mean shear modulus with an increasing lipid composition was identified through all stenosis sizes. However the inversion algorithm showed sensitivity to parameter variation leading to artefacts which disrupted both the elastograms and quantitative trends. As noise was increased up to a realistic level, the contrast was maintained between the fully fibrous and lipid plaques but lost between the interim compositions. Although incorporating a Butterworth filter improved the performance of the algorithm, restrictive filter thresholds resulted in a reduction of the sensitivity of the algorithm to composition and noise variation. Increasing the excitation frequency improved the techniques ability to image the magnitude of the shear modulus and identify a contrast between compositions.

In conclusion, whilst the technique has the potential to image the shear modulus of atherosclerotic plaques, future research will require the integration of a heterogeneous inversion algorithm.

1. Introduction

Cardiovascular diseases (CVD) were responsible for 31% of global mortalities in 2011 (Mendis et al., 2011). The root cause of the majority these deaths was atherosclerosis (Go et al., 2014). The pathogenesis of atherosclerosis is complex. The primary manifestation of atherosclerosis is an accumulation of lipid in the vascular wall caused by endothelial dysfunction (VanEpps and Vorp, 2007). However factors such as inflammation and biomechanics play a crucial role in the development of the disease (Libby et al., 2002). The rupture of a plaque may be associated with severe clinical events such as heart attack and stroke. The severity of an atherosclerotic plaque and the decision to refer the patient for surgery is based upon symptoms of ischemia and a measurement of the reduction in lumen diameter, known as a stenosis (Packard and Libby, 2008).

The outcome of surgical intervention via carotid endarterectomy, underwent analysis in the North American Symptomatic Carotid Endarterectomy Trial (NASCET) and European Carotid Surgery Trial (ECST). Rothwell et al. (2003) pooled this data and found an 18.7% absolute risk reduction, 5 years post-surgery, for stenoses between 70% and 99%. This statistic demonstrates that approximately 5 endarterectomies are required to prevent the death or stroke of 1 patient. The economic burden of CVD is estimated to be $315 billion in the USA and £19 billion in the UK (Townsend et al., 2012; Go et al., 2014).

A plaques vulnerability to rupture is associated with a number of factors including the size and consistency of the lipid pool, the thickness and mechanical properties of the fibrous cap, inflammation and fatigue in the fibrous cap (Falk et al., 1995). Research is focussed on more definitive diagnostic techniques including, imaging of the plaque composition (Corti and Fuster, 2011), molecular imaging (Mulder et al., 2014), imaging the tissue stiffness (De Korte et al., 2011) and imaging plaque stresses, known as patient specific modelling (Hoskins and Hardman, 2009).

Elastography is the overarching term given to elasticity imaging, using a combination of techniques to mechanically excite the tissue and modalities to image the response (Sarvazyan et al., 2011). An inversion algorithm is required to invert an image of displacement into an elastogram of the mechanical properties. Magnetic resonance elastography images the propagation of harmonic, low frequency, mechanical shear waves (Muthupillai et al., 1995). Arterial wall stiffness has been extracted using the Moens-Korteweg equation (Woodrum et al., 2006) and been applied to ex-vivo porcine aortas (Woodrum et al., 2009; Xu et al., 2012) and in-vivo abdominal aortas (Xu et al., 2013). The phase gradient inversion has identified changes in hypertensive aortic stiffness (Kolipaka et al., 2012). The local frequency estimation inversion has measured the relationship between aortic stiffness and age (Damughatla et al., 2015; Kenyhercz et al., 2015). The regional changes in shear modulus through ex-vivo porcine aortas have been measured by Zhang et al. (2016). Other studies have utilised interference elastography to visualise waves in the femoral artery (Zheng et al., 2007) and Fourier decomposed wave reflections to assess stenosis sizes in arterial phantoms (Woodrum et al., 2006).

The use of finite element analysis (FEA) is common across the modalities of elastography. It is primarily used as a method of inversion and a selection of studies have used FEA to invert strain images through atherosclerosis (Franquet et al., 2013; Bertoglio et al., 2014). FEA has also been used to create synthetic data sets to assess inversion algorithms (Van Houten et al., 2001; Miller et al., 2015) and explore the sensitivity of technique parameters (Chen et al., 2005). Baldewsing et al. (2004) and Doherty et al. (2013) assessed the application of ultrasound elastography to atherosclerosis by varying the geometric and mechanical properties within finite element models.

Measuring arterial stiffness is well established (Parker, 2009), however the term ‘stiffness’ is used as an overarching term for arterial characteristics that change with response to age or

disease (Hamilton et al., 2007). Imaging the specific mechanical properties of arteries is far less wide-spread, the literature contains conflicting results (Barrett et al., 2009) and vasculature-specific experimental data is required (Holzapfel et al., 2014). The parameters of constitutive models for arterial tissue can be extracted using mechanical testing (Holzapfel et al., 2000; Holzapfel et al., 2005). The documentation of the viscoelastic properties of healthy and diseased human arterial tissue is extremely limited. The well cited studies by Loree et al. (1994) and Lee et al. (1991) document the dynamic analysis and viscoelastic properties from ex-vivo samples of the lipid pool and fibrous cap. Viscoelastic properties have been extracted from in-vivo pressure displacement data by Valdez-Jasso et al. (2011). In recent years ultrasound elastography has shown promising results in quantifying the mechanical properties of atherosclerotic plaques (De Korte et al., 2011).

A preliminary computational investigation into the variation of the MRE steady state shear wave response through atherosclerotic plaques was undertaken by Thomas-Seale et al. (2011). The aim of this paper is to investigate the potential for MRE to image the shear modulus of atherosclerotic plaques through synthetic datasets.

2. Method

2.1 Finite Element Analysis

A direct solution, steady state FEA (Abaqus/CAE, Dassault Systèmes Simulia Corp., Providence, Rhode Island, USA) was applied to allow extraction of a complex wave image, analogous to the first harmonic of Fourier transformed experimental phase images.

The 3D geometry (Rhinoceros, McNeel, Seattle, Washington, USA) is displayed in Fig. 1 and Table 1. A plaque and vessel wall was embedded in a block of homogeneous tissue to replicate the transmission of shear waves in-vivo. The global axes and nomenclature are

depicted in Fig. 1a and 1b. The region of interest (ROI) is defined as the atherosclerotic plaque.

The dimensions of the plaque were based upon a cosine function (Eq. 1), the severity of the stenosis (Eq. 2) and 100% eccentricity (Eq. 3) (Ahmed and Giddens, 1983; Tang et al., 2004). The nomenclature is displayed in Fig. 1 and defined as follows; radius R_0, healthy lumen diameter ϕ_0, stenosis S and the diameter of the narrowest section ϕ_s. At a distance z along the vessel, where z_1 and z_2 are both ends of the stenosis and $R(z)$ is the radius of the vessel. The eccentricity is defined as E_c and e is the distance between the centre point of the vessel and lumen.

$$R(z) = R_0 - SR_0 \left\{1 - \cos\left[2\pi\left(z - z_1\right)/\left(z_2 - z_1\right)\right]\right\}/2 \quad (1)$$

$$S = \left(\phi_0 - \phi_s\right)/\phi_0 \times 100\% \quad (2)$$

$$E_c = e/\left[\left(\phi_0 - \phi_s\right)/2\right] \times 100\% \quad (3)$$

The disease development was modelled by varying the stenosis size and incremental changes in the spherical lipid pool volume. The lipid pool sphere was absent for the fully fibrous and fully lipid plaque geometries. The fibrous cap was modelled as 0.25mm (Loree et al., 1992). The geometry was meshed using hybrid and acoustic, linear, tetrahedron and hexahedron elements. The ROI was meshed using an element edge length of 0.5mm. Propagating away from the ROI the element edge length was gradually increased up to 2mm.

The blood was modelled as static and assigned acoustic properties (Hoskins, 2007). The soft tissues were modelled as isotropic, Hookean, viscoelastic materials with a density of 1047kgm^{-3} (Hoskins, 2010) and a Poisson's ratio of 0.5 (Fung, 1993). The viscoelasticity was represented by the dynamic shear modulus G; composed of the storage G' and loss modulus G'' (Eq. 4). The dynamic modulus can be defined by the shear modulus μ, shear viscosity η and frequency ω using a rheological model.

$$G(\omega) = G'(\omega) + iG''(\omega) \tag{4}$$

The viscoelastic properties of human arteries were taken from the most applicable research available; these are summarised in Table 2. The material properties for the healthy and diseased arterial wall, excluding the fibrous cap and lipid pool, were taken from the Neo-Hookean hyperelastic model outlined by Holzapfel et al. (2002). This constitutive model behaves like an elastic solid under small deformations (Bower, 2010). For these tissues the viscoelasticity was modelled using the Voigt model (Eq. 5 - 7). The shear viscosity was fixed at 80Pas (Valdez-Jasso et al., 2011).

$$G_{Voigt}(\omega) = \mu + i\omega\eta \tag{5}$$

$$G_{Voigt}'(\omega) = \mu \tag{6}$$

$$G_{Voigt}''(\omega) = \omega\eta \tag{7}$$

The surrounding tissue was given the viscoelastic properties of muscle (Klatt et al., 2010). The values of the shear modulus and shear viscosity for the lipid pool and fibrous cap were approximated by extrapolating the low frequency investigations of Loree et al. (1994), for a 0% cholesterol lipid, and Lee et al. (1991), for a cellular fibrous cap, into the frequency range used in this study. The shear moduli of these extrapolated values are comparable to those utilised by Holzapfel et al. (2002). The Maxwell model (Eq. 8 - 10) was used to represent the viscoelastic behaviour of the surrounding tissue, fibrous cap and lipid pool, due to the frequency dependence of the storage modulus demonstrated in the cited studies (Lee et al., 1991; Loree et al., 1994; Klatt et al., 2010).

$$G_{Maxwell}(\omega) = \frac{i\omega\eta\mu}{\mu + i\omega\eta} \tag{8}$$

$$G_{Maxwell}'(\omega) = \frac{\omega^2\eta^2\mu}{\mu^2 + \omega^2\eta^2} \tag{9}$$

$$G_{Maxwell}''(\omega) = \frac{\omega\eta\mu^2}{\mu^2 + \omega^2\eta^2} \tag{10}$$

Equations (11) and (12) define the Voigt and Maxwell model in terms of the loss angle, δ. Under small oscillatory loads, the loss angle describes the response of a viscoelastic material. The loss angle is defined as the arctangent of the loss to storage modulus (Fulcher et al., 2009). When the stress and strain are in phase, the material response is purely elastic and the loss angle is 0° (Barnes et al., 1989). When the stress and strain are out of phase, the material response in purely viscous and the loss angle is 90° (Barnes et al., 1989).

$$\delta_{Voigt} = a\tan\frac{\omega\eta}{\mu} \tag{11}$$

$$\delta_{Maxwell} = a\tan\frac{\mu}{\omega\eta} \tag{12}$$

The Voigt model has shown a good correlation to in-vivo arterial pressure-area dynamics (Valdez-Jasso et al., 2011). The storage modulus shows no dependence on excitation frequency and the loss modulus increases with frequency. Hence the Voigt model demonstrates an increasing loss angle with frequency, and the material response becomes more viscous. The loss angle of the Maxwell model, as applied to the surrounding tissue, lipid pool and fibrous cap, peaks at $\omega = \mu/\eta$. Above this frequency the decreasing loss modulus dominates the loss angle and makes the tissue behave more elastically with frequency.

The load nodes were isolated on the top surface of the model, shown in Fig. 1c. Harmonic, shear wave excitation was simulated using a sinusoidal load of $6\text{x}10^{-4}$N, applied parallel to the Z axis. The excitation frequency was varied between 50Hz and 200Hz. Symmetric boundary conditions were applied to the outer faces of the surrounding tissue, except the loading surface.

2.2 Inversion Algorithm

The displacement was extracted using a pixel size of $1mm^2$ through an imaging plane parallel to the X and Y axes. The displacement was averaged over a 2mm slice thickness, centred on the plaque, synonymous to an MRI voxel. Noise was added to the simulated data using the method outlined by Miller et al. (2015). The standard deviation of the signal σ_{signal}, was calculated using the real and imaginary wave amplitudes through the ROI. The distribution was modelled as Gaussian with a zero mean and standard deviation, σ_{noise}, derived by (Eq. 13), where $1\% \leq N \geq 20\%$.

$$\sigma_{noise} = N\% \cdot \sigma_{signal} \tag{13}$$

The displacement data was inverted into an elastogram using the Helmholtz algorithm (Eq. 14) (MATLAB R2011a, MathWorks, Natick, Massachusetts, USA). The derivation of this algorithm is described by Klatt et al. (2006). The dynamic shear modulus $G(\omega)$, was yielded by the Fourier transformed complex displacement U, wave excitation frequency ω and tissue density ρ. The Laplacian, $\nabla^2 U$, was calculated from second order spatial derivatives (Eq. 15). The dynamic shear modulus may be expressed in terms of the shear modulus μ and shear viscosity η using a rheological model. In this study the Voigt model was utilised (Eq. 5).

$$G(\omega) = \frac{-\rho\omega^2 U}{\nabla^2 U} \tag{14}$$

$$\nabla^2 U = \frac{\partial^2 u}{\partial x^2} + \frac{\partial^2 u}{\partial y^2} \tag{15}$$

A 2D Butterworth filter was used to suppress noise and compression wave components (Klatt et al., 2007; Clayton et al., 2011). The shear modulus formed the focus of this study; it is displayed in elastograms and as a spatially averaged value through the ROI using the mean of

20 noisy cycles. Unless explicitly stated the technique parameters were fixed at $N = 2\%$, 100Hz with filter thresholds of 5m^{-1} and 1000000m^{-1}.

3. Results

The wave images of Fig. 2 show that as the composition of the plaque become more lipid, the wave displacement through the low shear modulus material becomes visible. Although the geometry of the lipid pools can-not be identified in the elastograms, the decrease in the shear modulus can be seen through the stenosis as the lipid composition increases. The wave images of Fig. 3 display decreasing wavelengths and increasing attenuation with increasing frequency. The shear moduli through the elastograms increase with frequency. This observation is complemented by Fig. 4c.

All data sets in Fig. 4 show a contrast between the fully fibrous and lipid compositions. The magnitude of the mean shear modulus, the amount of contrast and the smoothness of the trend is degraded by the increase in noise. Figure 4a shows that at $N = 2\%$, and a frequency of 100Hz, there is a contrast between the incremental lipid volumes through all stenosis sizes. At $N = 10\%$ and $N = 20\%$ the fully fibrous compositions maintain a higher mean shear modulus than the fully lipid compositions, however the incremental decrease in contrast is lost. Table 3 omits the effects of filters and displays the raw shear modulus variation with N and plaque composition. Both Table 3 and Fig. 4a show degradation in contrast between compositions with increasing noise. The predicted shear moduli are one or two orders of magnitude lower than the simulated shear moduli.

Figure 4b shows that the 5m^{-1} to 1000000m^{-1} and 10m^{-1} to 1000m^{-1} filter ranges improve the performance of the algorithm in terms of magnitudes and contrast between compositions. As the filter thresholds are narrowed to between 15m^{-1} and 500m^{-1}, the distinctive wave behaviour between compositions is over smoothed and the magnitudes and contrasts are

reduced. At the narrowest filter thresholds, similar to those found in experimental work (Klatt et al., 2007), the algorithm becomes insensitive to any variation in noise.

4. Discussion

Harmonic wave propagation through an isotropic, homogeneous, incompressible, linear elastic medium in the absence of body forces can be described by the Helmholtz equation (Manduca et al., 2001). The limitations of the inversion algorithm are discussed in depth in (Barbone and Gokhale, 2004; Papazoglou et al., 2008). In this study, the discrete and noisy data through the heterogeneous application created artefacts, which can be seen in Fig. 2.

Through a homogeneous medium, harmonic wave propagation will lead to a displacement and Laplacian term of opposite polarity. With reference to Eq. (14), this generates a positive and thus real dynamic shear modulus. In discrete data the Laplacian is calculated from the second order spatial gradients, Eq. (15), using two pixels adjacent to the pixel of interest. Inhomogeneities through the medium, or step changes in the wave behaviour, change the magnitude of this second order derivative. This can lead to errors in the shear moduli. This exaggeration of gradients can be seen by comparing the visibly low level of noise in the wave images of Fig 2. to the pronounced noise through the corresponding elastograms. Most crucially, if the displacement and Laplacian are of the same polarity an impossible, negative dynamic shear modulus is yielded. This numerical limitation was demonstrated by Thomas-Seale (2015). In these cases the impossible values are equated to zero.

Along boundaries, similar artefacts can be identified as a line of over or underestimated pixels. Beyond the X axis edge of the elastogram, there is no information. This reduces the size of the Laplacian and creates an artefact of overestimated shear moduli. Since there is minimal wave propagation parallel to the Y axis, there are no gradients and therefore no artefacts adjacent to this edge. Along the edge of the lumen, there is an interface between the

blood and artery wall. Within 1mm there is also an interface between the artery wall and surrounding tissue. On the upper interface there is an underestimated artefact of two pixels deep. This is generated by the inflated spatial derivatives adjacent to the zero displacement of the blood. On the lower interface there are lines of both underestimated pixels and overestimated pixels. Observing the wave images of Fig. 2, the most pertinent difference between the wave intersecting the upper and lower interface is the phase. Figure 3 shows that the location of the zero pixel artefacts and the magnitude of the artefacts above and below the lumen, change with frequency. It can be concluded that these artefacts show a dependency on the phase of the wave. This reflection suggests that a multi-frequency inversion could alleviate the effect of these artefacts.

Figure 3 and 4c show an increase in shear modulus with frequency. MRE excitation frequency is strongly linked to resolution (Sinkus et al., 2000; Parker et al., 2005). The increase in technique resolution with excitation frequency can be identified by the emerging visibility of the lipid pool through the wave image at higher frequencies. As the wavelength decreases, the contrast and detectability of inclusions are increased. Only a fraction of the wave motion is captured within the plaque, therefore the algorithm can-not interpret the true shear modulus. At 200Hz the wave propagation below the lumen is highly attenuated and the amplitude oscillates around $\pm 5\mu m$. This low amplitude combined with a 2mm element edge and voxel of resolution $1mm^2$ x 2mm generated a discretisation error which followed through to errors in the shear moduli.

The degradation of the results of Table 3 and Fig. 4a with increasing noise stems from the disruption in the clarity of the wave gradients and hence the ability of the algorithm to calculate the shear modulus. Noise, increases step changes in the wave displacement and hence exasperates the artefacts. This conclusion is supported by the increase in standard deviation with noise, relative to the mean, for the majority of compositions in Table 3.

The Butterworth filter smooths out noise and compression wave components. Under pure shear excitation, MRE through an incompressible medium allows compressional effects to be neglected (Mariappan et al., 2010). In this simulated study the only interference with the shear wave propagation are refracted and reflected waves, therefore noise was the dominant component to be filtered.

The juxtaposition between the fact that filters smooth the data and therefore improve the function of the inversion algorithm, and the fact the essence of this study lies in identifying the difference in wave behaviour between the heterogeneous compositions, results in an oxymoron. Thomas-Seale (2015) varied the thresholds through their full range and concluded that over filtering of the wave images, through this heterogeneous application, can manipulate the results. The filter thresholds could be optimised to this application and each frequency, however even under these idealised conditions, the inversion algorithm is ill-suited to this highly heterogeneous application. Attempting to improve its function by filtering also smooths the essential contrast between compositions; this is shown in Fig. 4b.

The Helmholtz inversion algorithm has shown extreme sensitivity throughout this application. The location, presentation and severity of artefacts have demonstrated a dependence on noise, inhomogenieties and excitation frequency. This has created a level of unpredictability in the analysis seen by the artefacts in the elastograms and sporadic high and low values throughout the quantitative trends. In Fig. 4c, this is noticeable through the 200Hz, maximum noise analysis due to the combination of high noise and large gradients. In conclusion, although this technique shows promise, identifying accurate mechanical properties and contrast between plaque compositions hinges on developing a more applicable, heterogeneous inversion algorithm.

This research, has allowed assessment of the technique and identification of the areas that require development. However the idealised nature of the study is limiting. It has focussed on

a system with simplified parameters and has neglected the wave interaction with surrounding organs and the cardiac cycle. The Voigt and Maxwell models are arguably not sophisticated enough to fully describe the mechanical behaviour of arterial tissue and they are also not ideal under wide frequency ranges (Yasar et al., 2013). The voxel resolution in this study was idealised. Experimentally, an increase in resolution results in a decrease of signal to noise ratio (McRobbie, 2007), therefore increasing the resolution will compound the limitations seen in this research. This study has neglected the stiffness created by the shape of the ROI. There is potential here to develop an inversion algorithm that is more applicable to the cylindrical form of arterial structures. This concept has been broached in the work of Kolipaka et al. (2009) through bounded media. Realistic methods of extracting and modelling noise vary throughout MRE literature (Papazoglou et al., 2008; McGee et al., 2011). The limitation of the method applied in this research (Miller et al., 2015), is that the standard deviation, and hence noise level, changes with composition and frequency.

5. Conclusion

Simulated MRE through atherosclerotic plaques has allowed preliminary analysis of the technique. A contrast between plaque composition and size was identified through the mean shear modulus. However the inversion algorithm was sensitive to parameter variation and constrained by the limitations of the discrete, noisy and heterogeneous data in this study. Whilst filtering improved its accuracy, narrow filter thresholds also reduced the essential contrast between the compositions. An increase in frequency, improved the resolution of the technique in terms of magnitude and contrast. An inversion algorithm applicable to heterogeneous tissue is required to continue this research.

Acknowledgements

This research was funded by the Engineering and Physical Sciences Research Council.

Word Count: 3486

Conflict of Interest Statement

There are no personal or financial conflicts of interest associated with this study.

References

Ahmed, S. A., Giddens, D. P. 1983. Velocity-measurements in steady flow through axisymmetric stenoses at moderate Reynolds-numbers. Journal of Biomechanics, 16, 505-516.

Baldewsing, R. A., De Korte, C. L., Schaar, J. A., Mastik, F., Van Der Steen, A. F. W. 2004. Finite element modeling and intravascular ultrasound elastography of vulnerable plaques: parameter variation. Ultrasonics, 42, 723-729.

Barbone, P. E., Gokhale, N. H. 2004. Elastic modulus imaging: on the uniqueness and nonuniqueness of the elastography inverse problem in two dimensions. Inverse Problems, 20, 283-296.

Barnes, H. A., Hutton, J. F., Walters, K. 1989. An Introduction to Rheology, Elsevier, Oxford, UK.

Barrett, S. R. H., Sutcliffe, M. P. F., Howarth, S., Li, Z. Y., Gillard, J. H. 2009. Experimental measurement of the mechanical properties of carotid atherothrombotic plaque fibrous cap. Journal of Biomechanics, 42, 1650-1655.

Bertoglio, C., Barber, D., Gaddum, N., Valverde, I., Rutten, M., Beerbaum, P., Moireau, P., Hose, R., Gerbeau, J. F. 2014. Identification of artery wall stiffness: In vitro validation and in vivo results of a data assimilation procedure applied to a 3D fluid-structure interaction model. Journal of Biomechanics, 47, 1027-1034.

Bower, A. F. 2010. Applied Mechanics of Solids, CRC Press, Boca Raton, Florida.

Chen, Q. S., Ringleb, S. I., Manduca, A., Ehman, R. L., An, K. N. 2005. A finite element model for analyzing shear wave propagation observed in magnetic resonance elastography. Journal of Biomechanics, 38, 2198-2203.

Clayton, E. H., Garbow, J. R., Bayly, P. V. 2011. Frequency-dependent viscoelastic parameters of mouse brain tissue estimated by MR elastography. Physics in Medicine and Biology, 56, 2391-2406.

Corti, R., Fuster, V. 2011. Imaging of atherosclerosis: magnetic resonance imaging. European Heart Journal, 32, 1709-1719.

Damughatla, A. R., Raterman, B., Sharkey-Toppen, T., Jin, N., Simonetti, O. P., White, R. D., Kolipaka, A. 2015. Quantification of aortic stiffness using MR elastography and its comparison to MRI-based pulse wave velocity. Journal of Magnetic Resonance Imaging, 41, 44-51.

De Korte, C. L., Hansen, H. H. G., Van Der Steen, A. F. W. 2011. Vascular ultrasound for atherosclerosis imaging. Interface Focus, 1, 565-575.

355 Doherty, J. R., Dumont, D. M., Trahey, G. E., Palmeri, M. L. 2013. Acoustic radiation force
356 impulse imaging of vulnerable plaques: a finite element method parametric analysis.
357 Journal of Biomechanics, 46, 83-90.

358 Falk, E., Shah, P. K., Fuster, V. 1995. Coronary plaque disruption. Circulation, 92, 657-671.

359 Franquet, A., Avril, S., Le Riche, R., Badel, P., Schneider, F. C., Boissier, C., Favre, J. P.
360 2013. Identification of the in vivo elastic properties of common carotid arteries from
361 MRI: A study on subjects with and without atherosclerosis. Journal of the Mechanical
362 Behavior of Biomedical Materials, 27, 184-203.

363 Fulcher, G. R., Hukins, D. W. L., Shepherd, D. E. T. 2009. Viscoelastic properties of bovine
364 articular cartilage attached to subchondral bone at high frequencies. BMC
365 Musculoskeletal Disorders, 10, 61.

366 Fung, Y. C. 1993. Biomechanics: Mechanical Properties of Living Tissues, Springer-Verlag,
367 New York.

368 Go, A. S., Mozaffarian, D., Roger, V. L., Benjamin, E. J., Berry, J. D., Blaha, M. J., Dai, S.
369 F., Ford, E. S., Fox, C. S., Franco, S., Fullerton, H. J., Gillespie, C., Hailpern, S. M.,
370 Heit, J. A., Howard, V. J., Huffman, M. D., Judd, S. E., Kissela, B. M., Kittner, S. J.,
371 Lackland, D. T., Lichtman, J. H., Lisabeth, L. D., Mackey, R. H., Magid, D. J.,
372 Marcus, G. M., Marelli, A., Matchar, D. B., Mcguire, D. K., Mohler, E. R., Moy, C.
373 S., Mussolino, M. E., Neumar, R. W., Nichol, G., Pandey, D. K., Paynter, N. P.,
374 Reeves, M. J., Sorlie, P. D., Stein, J., Towfighi, A., Turan, T. N., Virani, S. S., Wong,
375 N. D., Woo, D., Turner, M. B. 2014. Heart disease and stroke statistics - 2014 update.
376 A report from the American Heart Association. Circulation, 129, E28-E292.

377 Hamilton, P. K., Lockhart, C. J., Quinn, C. E., Mcveigh, G. E. 2007. Arterial stiffness:
378 clinical relevance, measurement and treatment. Clinical Science, 113, 157-170.

379 Holzapfel, G. A., Mulvihill, J. J., Cunnane, E. M., Walsh, M. T. 2014. Computational
380 approaches for analyzing the mechanics of atherosclerotic plaques: A review. Journal
381 of Biomechanics, 47, 859-869.

382 Holzapfel, G. A., Schulze-Bauer, C. a. J., Stadler, M. 2000. Mechanics of angioplasty: Wall,
383 balloon, and stent. In: Casey, J., Bao, G. (Eds.) Mechanics in Biology. The American
384 Society of Mechanical Engineers, New York.

385 Holzapfel, G. A., Sommer, G., Gasser, C. T., Regitnig, P. 2005. Determination of layer-
386 specific mechanical properties of human coronary arteries with nonatherosclerotic
387 intimal thickening and related constitutive modeling. American Journal of
388 Physiology-Heart and Circulatory Physiology, 289, H2048-H2058.

389 Holzapfel, G. A., Stadler, M., Schulze-Bauer, C. a. J. 2002. A layer-specific three-
390 dimensional model for the simulation of balloon angioplasty using magnetic

391 resonance imaging and mechanical testing. Annals of Biomedical Engineering, 30,
392 753-767.

393 Hoskins, P. R. 2007. Physical properties of tissues relevant to arterial ultrasound imaging and
394 blood velocity measurement. Ultrasound in Medicine and Biology, 33, 1527-1539.

395 Hoskins, P. R. 2010. Elastography. In: Hoskins, P. R., Martin, K., Thrush, A. (Eds.)
396 Diagnostic Ultrasound: Physics and Equipment. 2nd ed., Cambridge University Press,
397 Cambridge, UK.

398 Hoskins, P. R., Hardman, D. 2009. Three-dimensional imaging and computational modelling
399 for estimation of wall stresses in arteries. British Journal of Radiology, 82, S3-S17.

400 Kenyhercz, W. E., Raterman, B., Illapani, V. S. P., Dowell, J., Mo, X., White, R. D.,
401 Kolipaka, A. 2015. Quantification of aortic stiffness using magnetic resonance
402 elastography: measurement reproducibility, pulse wave velocity comparison, changes
403 over cardiac cycle, and relationship with age. Magnetic Resonance in Medicine, (In
404 Print).

405 Klatt, D., Asbach, P., Rump, J., Papazoglou, S., Somasundaram, R., Modrow, J., Braun, J.,
406 Sack, I. 2006. In vivo determination of hepatic stiffness using steady-state free
407 precession magnetic resonance elastography. Investigative Radiology, 41, 841-848.

408 Klatt, D., Hamhaber, U., Asbach, P., Braun, J., Sack, I. 2007. Noninvasive assessment of the
409 rheological behavior of human organs using multifrequency MR elastography: a study
410 of brain and liver viscoelasticity. Physics in Medicine and Biology, 52, 7281-7294.

411 Klatt, D., Papazoglou, S., Braun, J., Sack, I. 2010. Viscoelasticity-based MR elastography of
412 skeletal muscle. Physics in Medicine and Biology, 55, 6445-6459.

413 Kolipaka, A., Mcgee, K. P., Manduca, A., Romano, A. J., Glaser, K. J., Araoz, P. A., Ehman,
414 R. L. 2009. Magnetic resonance elastography: inversions in bounded media. Magnetic
415 Resonance in Medicine, 62, 1533-1542.

416 Kolipaka, A., Woodrum, D., Araoz, P. A., Ehman, R. L. 2012. MR elastography of the in
417 vivo abdominal aorta: A feasibility study for comparing aortic stiffness between
418 hypertensives and normotensives. Journal of Magnetic Resonance Imaging, 35, 582-
419 586.

420 Lee, R. T., Grodzinsky, A. J., Frank, E. H., Kamm, R. D., Schoen, F. J. 1991. Structure-
421 dependent dynamic mechanical behaviour of fibrous caps from human atherosclerotic
422 plaques. Circulation, 83, 1764-1770.

423 Libby, P., Ridker, P. M., Maseri, A. 2002. Inflammation and atherosclerosis. Circulation,
424 105, 1135-1143.

Loree, H. M., Kamm, R. D., Stringfellow, R. G., Lee, R. T. 1992. Effects of fibrous cap thickness on peak circumferential stress in model atherosclerotic vessels. Circulation Research, 71, 850-858.

Loree, H. M., Tobias, B. J., Gibson, L. J., Kamm, R. D., Small, D. M., Lee, R. T. 1994. Mechanical properties of model atherosclerotic lesion lipid pools. Arteriosclerosis and Thrombosis, 14, 230-234.

Manduca, A., Oliphant, T. E., Dresner, M. A., Mahowald, J. L., Kruse, S. A., Amromin, E., Felmlee, J. P., Greenleaf, J. F., Ehman, R. L. 2001. Magnetic resonance elastography: Non-invasive mapping of tissue elasticity. Medical Image Analysis, 5, 237-254.

Mariappan, Y. K., Glaser, K. J., Ehman, R. L. 2010. Magnetic resonance elastography: a review. Clinical Anatomy, 23, 497-511.

Mcgee, K. P., Lake, D., Mariappan, Y., Hubmayr, R. D., Manduca, A., Ansell, K., Ehman, R. L. 2011. Calculation of shear stiffness in noise dominated magnetic resonance elastography data based on principal frequency estimation. Physics in Medicine and Biology, 56, 4291-4309.

Mcrobbie, D. W. 2007. MRI from Picture to Proton, Cambridge University Press, Cambridge, UK.

Mendis, S., Puska, P., Norrving, B. 2011. Global Atlas on Cardiovascular Disease and Control, World Health Organisation, Geneva.

Miller, R., Jiang, H., Mazumder, R., Cowan, B., Nash, M., Kolipaka, A., Young, A. Determining anisotropic myocardial stiffness from magnetic resonance elastography: a simulation study. In: Functional Imaging and Modelling of the Heart: 8th International Conference, FIMH 2015, June 25-17, 2015, The Netherlands: Springer, 346-354.

Mulder, W. J. M., Jaffer, F. A., Fayad, Z. A., Nahrendorf, M. 2014. Imaging and nanomedicine in inflammatory atherosclerosis. Science Translational Medicine, 6, 1-11.

Muthupillai, R., Lomas, D. J., Rossman, P. J., Greenleaf, J. F., Manduca, A., Ehman, R. L. 1995. Magnetic-resonance elastography by direct visualization of propagating acoustic strain waves. Science, 269, 1854-1857.

Packard, R. R. S., Libby, P. 2008. Inflammation in atherosclerosis: From vascular biology to biomarker discovery and risk prediction. Clinical Chemistry, 54, 24-38.

Papazoglou, S., Hamhaber, U., Braun, J., Sack, I. 2008. Algebraic Helmholtz inversion in planar magnetic resonance elastography. Physics in Medicine and Biology, 53, 3147-3158.

Parker, K. H. 2009. A brief history of arterial wave mechanics. Medical & Biological Engineering & Computing, 47, 111-118.

Parker, K. J., Taylor, L. S., Gracewski, S., Rubens, D. J. 2005. A unified view of imaging the elastic properties of tissue. Journal of the Acoustical Society of America, 117, 2705-2712.

Rothwell, P. M., Gutnikov, S. A., Warlow, C. P., European Carotid Surgery, T. 2003. Reanalysis of the final results of the European Carotid Surgery Trial. Stroke, 34, 514-523.

Sarvazyan, A., Hall, T. J., Urban, M. W., Fatemi, M., Aglyamov, S. R., Garra, B. S. 2011. An overview of elastography - an emerging branch of medical imaging. Current Medical Imaging Reviews, 7, 255-282.

Sinkus, R., Lorenzen, J., Schrader, D., Lorenzen, M., Dargatz, M., Holz, D. 2000. High-resolution tensor MR elastography for breast tumour detection. Physics in Medicine and Biology, 45, 1649-1664.

Tang, D. L., Yang, C., Kobayashi, S., Ku, D. N. 2004. Effect of a lipid pool on stress/strain distributions in stenotic arteries: 3-D fluid-structure interactions (FSI) models. Journal of Biomechanical Engineering - Transactions of the ASME, 126, 363-370.

Thomas-Seale, L. E. J. 2015. The Application of Magnetic Resonance Elastography to Atherosclerosis. Doctor of Philosophy, Thesis, The University of Edinburgh.

Thomas-Seale, L. E. J., Klatt, D., Pankaj, P., Roberts, N., Sack, I., Hoskins, P. R. 2011. A simulation of the magnetic resonance elastography steady state wave response through idealised atherosclerotic plaques. IAENG International Journal of Computer Science, 38, 394-400.

Townsend, N., Wickramasinghe, K., Bhatnagar, P., Smolina, K., Nichols, M., Leal, J., Luengo-Fernandez, R., Rayner, M. 2012. Coronary heart disease statistics 2012 edition, British Heart Foundation, London, UK.

Valdez-Jasso, D., Bia, D., Zocalo, Y., Armentano, R. L., Haider, M. A., Olufsen, M. S. 2011. Linear and nonlinear viscoelastic modeling of aorta and carotid pressure-area dynamics under in Vivo and ex vivo conditions. Annals of Biomedical Engineering, 39, 1438-1456.

Van Houten, E. E. W., Miga, M. I., Weaver, J. B., Kennedy, F. E., Paulsen, K. D. 2001. Three-dimensional subzone-based reconstruction algorithm for MR elastography. Magnetic Resonance in Medicine, 45, 827-837.

Vanepps, J. S., Vorp, D. A. 2007. Mechanopathobiology of atherogenesis: A review. Journal of Surgical Research, 142, 202-217.

Woodrum, D. A., Herrmann, J., Lerman, A., Romano, A. J., Lerman, L. O., Ehman, R. L. 2009. Phase-contrast MRI-based elastography technique detects early hypertensive changes in ex vivo porcine aortic wall. Journal of Magnetic Resonance Imaging, 29, 583-587.

Woodrum, D. A., Romano, A. J., Lerman, A., Pandya, U. H., Brosh, D., Rossman, P. J., Lerman, L. O., Ehman, R. L. 2006. Vascular wall elasticity measurement by magnetic resonance imaging. Magnetic Resonance in Medicine, 56, 593-600.

Xu, L., Chen, J., Glaser, K. J., Yin, M., Rossman, P. J., Ehman, R. L. 2013. MR elastography of the human abdominal aorta: A preliminary study. Journal of Magnetic Resonance Imaging, 38, 1549-1553.

Xu, L., Chen, J., Yin, M., Glaser, K. J., Chen, Q. S., Woodrum, D. A., Ehman, R. L. 2012. Assessment of stiffness changes in the ex vivo porcine aortic wall using magnetic resonance elastography. Magnetic Resonance Imaging, 30, 122-127.

Yasar, T. K., Royston, T. J., Magin, R. L. 2013. Wideband MR elastography for viscoelasticity model identification. Magnetic Resonance in Medicine, 70, 479-489.

Zhang, N., Chen, J., Yin, M., Glaser, K. J., Xu, L., Ehman, R. L. 2016. Quantification of regional aortic stiffness using MR elastography: A phantom and ex-vivo porcine aorta study. Magnetic Resonance Imaging, 34, 91-96.

Zheng, Y., Chan, Q. C. C., Li, G., Lam, E. Y., Yang, E. S. 2007. A study of femoral artery by twin drivers in magnetic resonance interference elastography. In: The 29th Annual International Conference of the IEEE Engineering in Medicine and Biology Society, Aug 22-26, 2007, Lyon, France, 2034-2037.

519 **List of Tables**

520 **Table 1.** The geometric parameters of the surrounding tissue, arterial wall and atherosclerotic
521 plaque components. The values are taken from the following references *(Schulze-Bauer et
522 al., 2003) and **(Loree et al., 1992). *(1 Column)*

523 **Table 2.** The material properties of the surrounding tissue, arterial wall, atherosclerotic
524 plaque components and blood. The values are taken from the following references *(Hoskins,
525 2010), **(Klatt et al., 2010), $^{+}$(Holzapfel et al., 2002), $^{++}$(Valdez-Jasso et al., 2011), $^{\#}$(Lee et
526 al., 1991), $^{\#\#}$(Loree et al., 1994), $^{\wedge}$(Hoskins, 2007). *(1 Column)*

527 **Table 3.** The mean predicted shear modulus through an 80% stenosis with variations in
528 composition and Gaussian noise. *(1.5 Columns)*

529

530

List of Figures

Figure 1 Rev. 2

Click here to download high resolution image

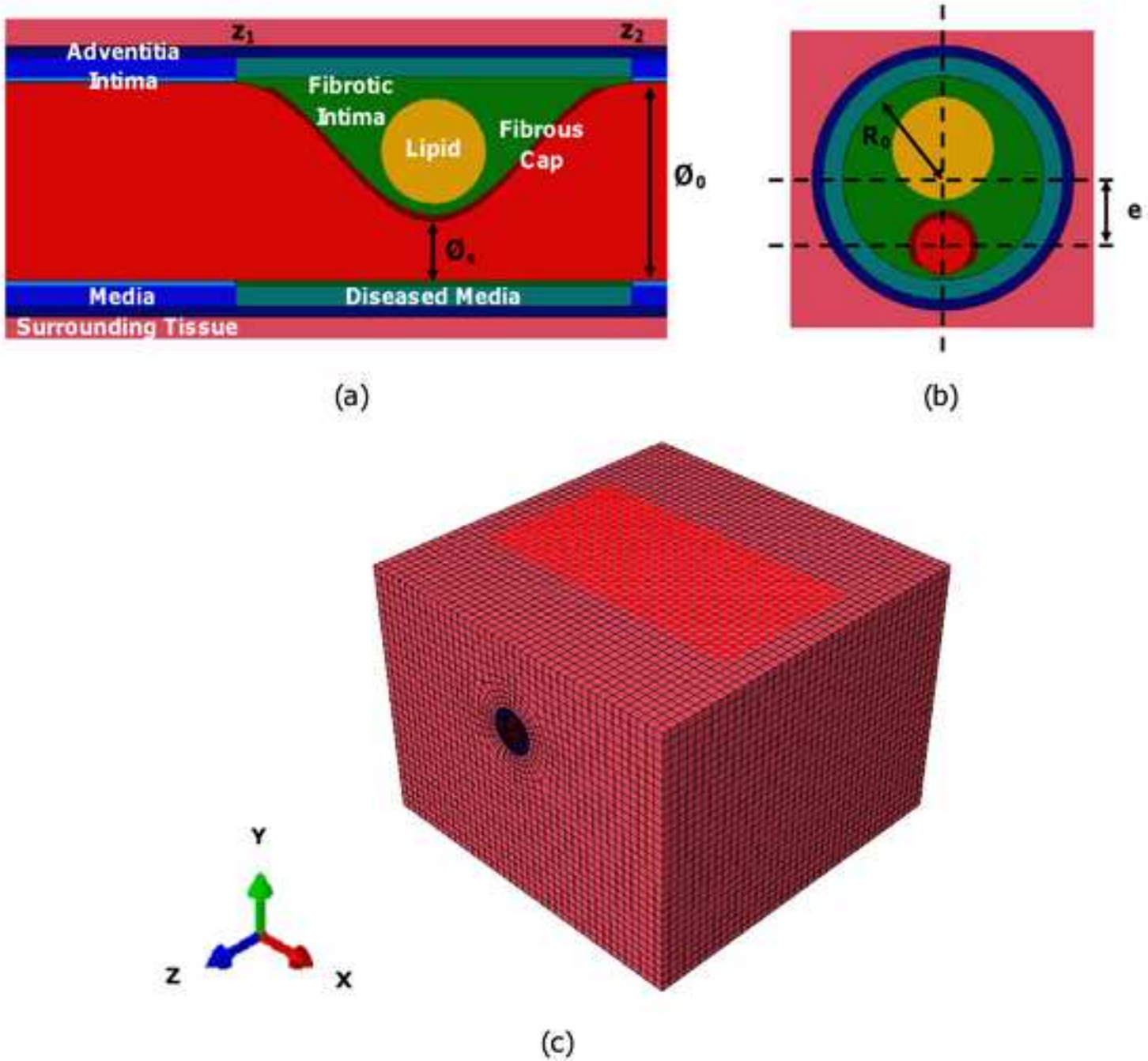

Figure 2 Rev. 2

Click here to download high resolution image

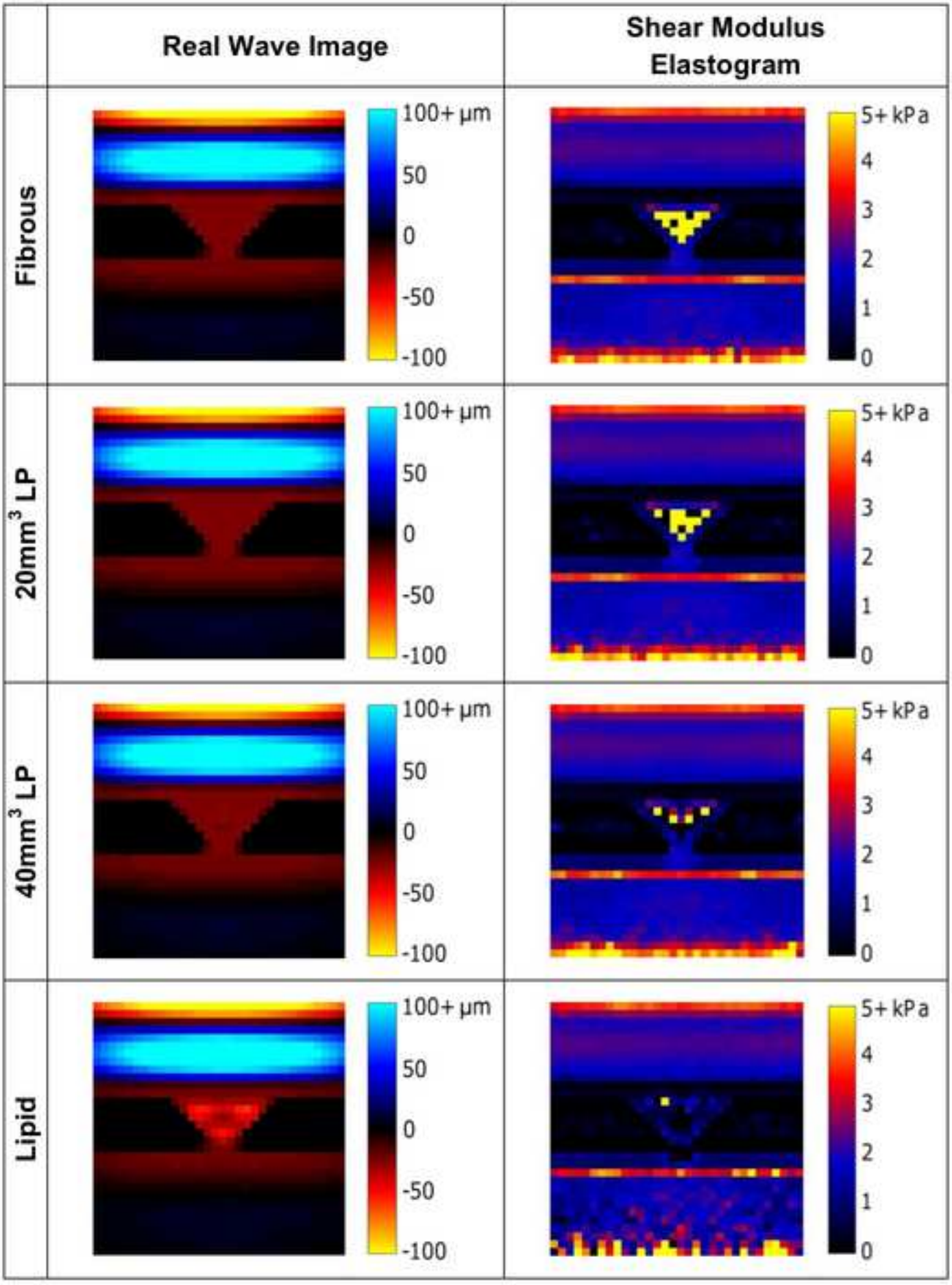

Figure 3 Rev. 2

Click here to download high resolution image

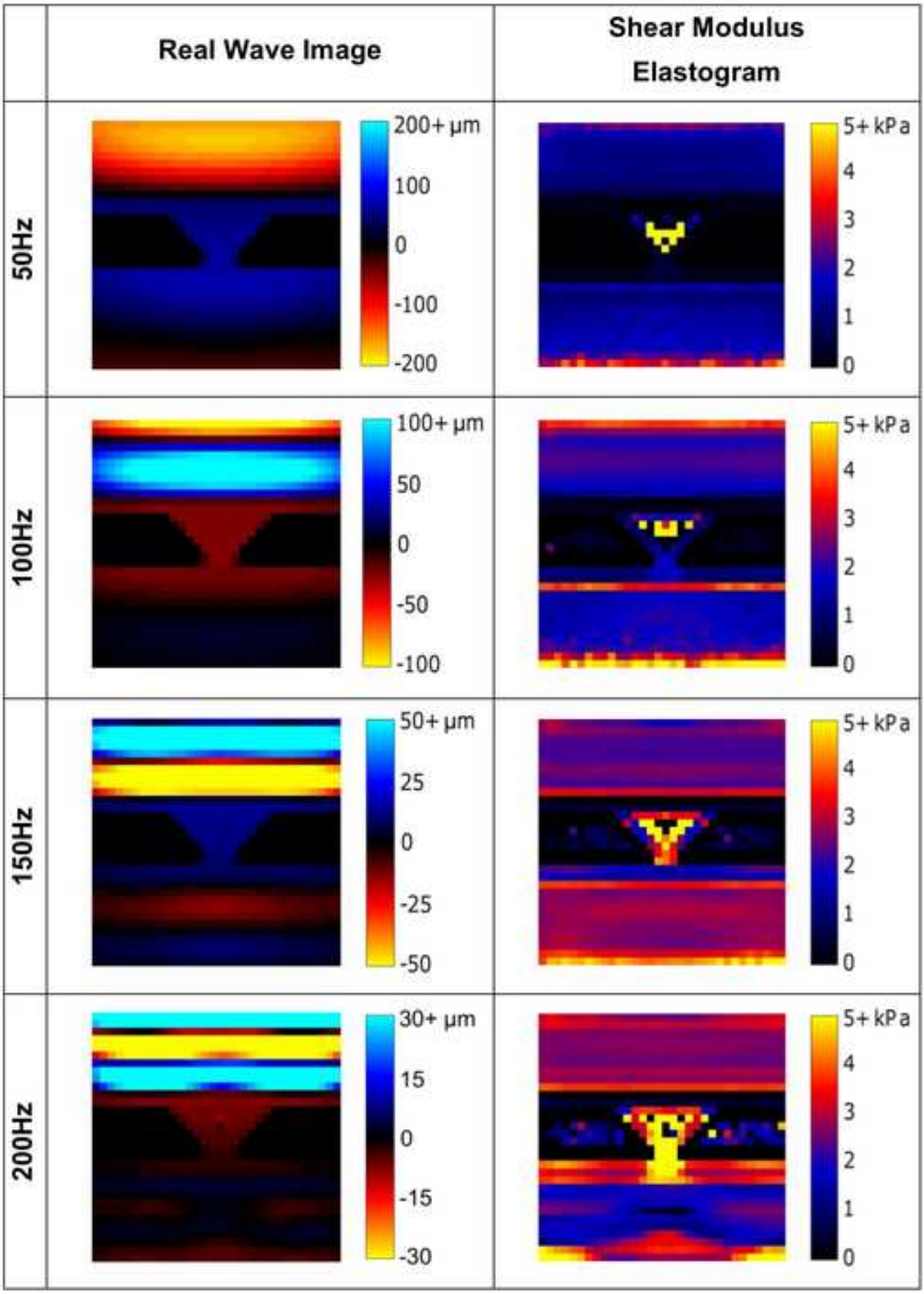

Figure 4 Rev. 2

Click here to download high resolution image

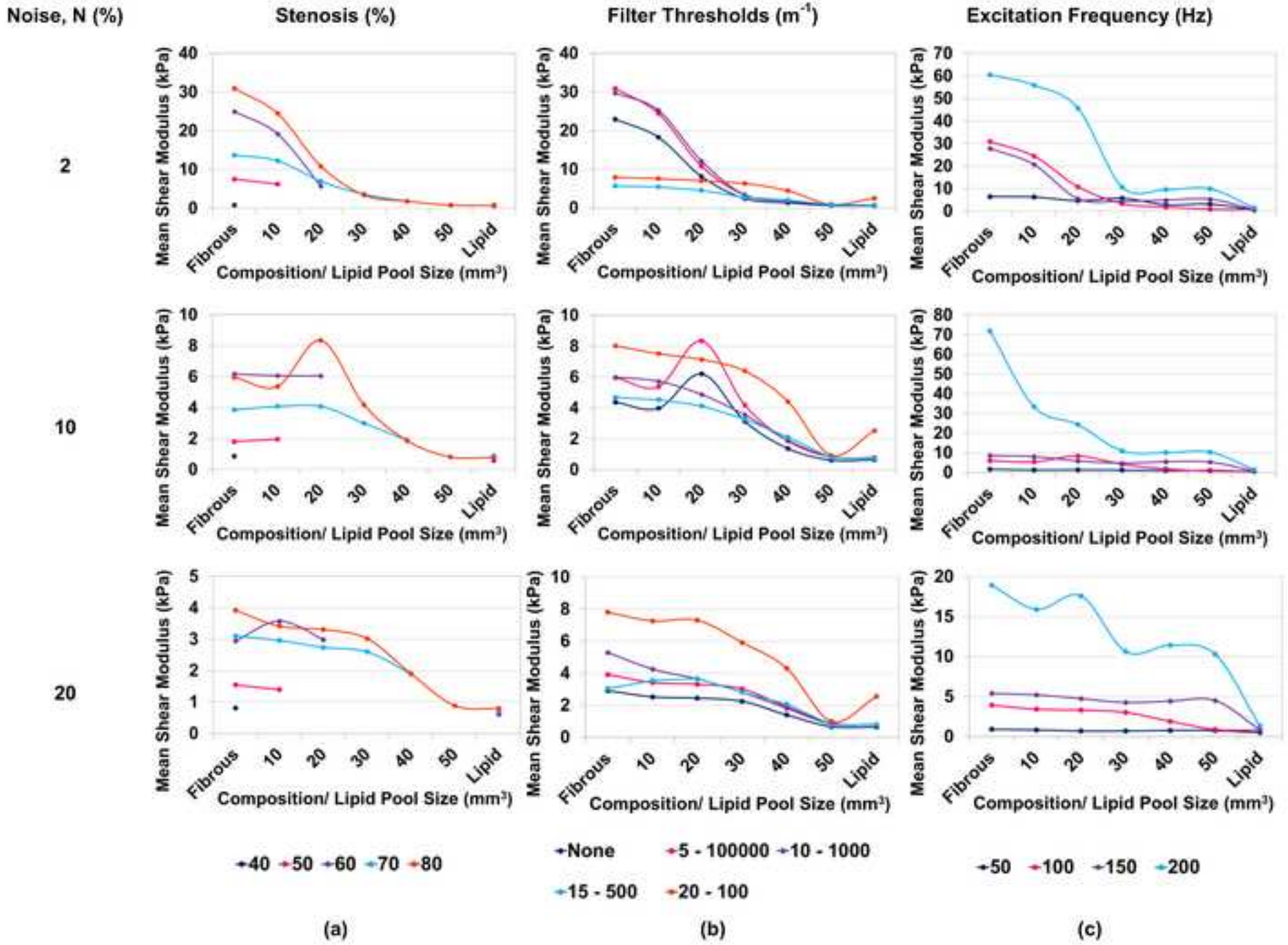

Table 1 Rev. 2

Tissue	Geometric Parameter	Value
Surrounding Tissue	Length	80.00 mm
	Width	80.00 mm
	Depth	60.00 mm
Stenosis	Length	14.52 mm
Intima	Inner Radius	3.63 mm*
	Thickness	0.17 mm*
Media	Inner Radius	3.80 mm*
	Thickness	0.73 mm*
Adventitia	Inner Radius	4.53 mm*
	Thickness	0.43 mm*
Fibrous Cap	Thickness	0.25/0.5/0.75mm**
Lipid Pool	Volume	0/10/20/30/40/50/ Total mm^3

Table 2 Rev. 2

Tissue	Density (kgm^{-3})	Shear Modulus (kPa)	Bulk Modulus (kPa)	Shear Viscosity (Pas)
Surrounding Tissue	1047*	2.3**	-	17.0**
Intima	1047*	150.0^{+}	-	80.0^{++}
Fibrotic Intima	1047*	221.0^{+}	-	80.0^{++}
Media	1047*	34.0^{+}	-	80.0^{++}
Diseased Media	1047*	757.0^{+}	-	80.0^{++}
Adventitia	1047*	50.0^{+}	-	80.0^{++}
Fibrous Cap	1047*	$208.4^{\#}$	-	$19820.0^{\#}$
Lipid	1047*	$0.1^{\#\#}$	-	$6.4^{\#\#}$
Blood	$1060^{\wedge}$	-	$2.67x10^{6\wedge}$	-

Table 3 Rev. 2

Noise, N (%)	Mean/Standard Deviation Predicted Shear Modulus (kPa)						
	Fibrous Plaque	Lipid Pool Volume					Lipid Plaque
		$10mm^3$	$20mm^3$	$30mm^3$	$40mm^3$	$50mm^3$	
Omitted	30.9	29.9	5.2	2.4	1.3	0.6	0.6
1	30.1/5.0	22.5/2.4	9.0/4.5	2.4/0.1	1.3/0.0	0.6/0.0	0.6/0.0
2	23.0/4.3	18.3/3.7	8.2/3.4	2.4/0.2	1.3/0.0	0.6/0.0	0.6/0.0
5	7.3/2.3	9.6/5.7	5.8/2.6	3.0/1.2	1.3/0.0	0.6/0.0	0.6/0.0
10	4.4/0.8	4.0/0.8	6.2/5.3	3.1/1.6	1.4/0.1	0.6/0.0	0.6/0.1
15	3.2/1.1	3.7/1.1	3.1/1.6	2.1/0.4	1.4/0.3	0.6/0.1	0.7/0.2
20	2.9/1.0	2.5/0.7	2.4/0.7	2.2/0.6	1.4/0.2	0.7/0.1	0.6/0.1
Mean Simulated Shear Modulus	**219.6**	**190.2**	**172.9**	**158.5**	**145.5**	**133.6**	**23.1**

Conflict of Interest Statement

There are no personal or financial conflicts of interest associated with this study.